

Nanoscale

Accepted Manuscript



This is an *Accepted Manuscript*, which has been through the Royal Society of Chemistry peer review process and has been accepted for publication.

Accepted Manuscripts are published online shortly after acceptance, before technical editing, formatting and proof reading. Using this free service, authors can make their results available to the community, in citable form, before we publish the edited article. We will replace this *Accepted Manuscript* with the edited and formatted *Advance Article* as soon as it is available.

You can find more information about *Accepted Manuscripts* in the [Information for Authors](#).

Please note that technical editing may introduce minor changes to the text and/or graphics, which may alter content. The journal's standard [Terms & Conditions](#) and the [Ethical guidelines](#) still apply. In no event shall the Royal Society of Chemistry be held responsible for any errors or omissions in this *Accepted Manuscript* or any consequences arising from the use of any information it contains.

Facile synthesis of high quality multi-walled carbon nanotubes on novel 3D

KIT-6: Application in high performance dye-sensitized solar cells

Jayaraman Balamurugan,^a Arumugam Pandurangan,^{b*} Nam Hoon Kim,^a Joong Hee Lee^{a,c*}

^a*Advanced Materials Institute of BIN Technology (BK21 plus Global) & Dept. of BIN Fusion Technology, Chonbuk National University, Jeonju, Jeonbuk 561-756, Republic of Korea.*

^b*Department of Chemistry, Institute of Catalysis and Petroleum Technology, Anna University, Chennai 600 025, India*

^c*Carbon Composite Research Centre, Department of Polymer & Nanoscience and Technology, Chonbuk National University Jeonju, Jeonbuk 561-756, Republic of Korea*

*Corresponding authors: E-Mail: pandurangan_a@yahoo.com (Arumugam Pandurangan)

Fax: +91-44-22200660; Tel: +91-44-22358653

E-Mail: jhl@jbnu.ac.kr (Joong Hee Lee)

Fax: +82 832702341; Tel: +82 832702342

Abstract

A novel hard templating strategy for the synthesis of high quality multi-walled carbon nanotubes (MWCNTs) with uniform diameter was developed. MWCNTs were successfully synthesized through chemical vapour deposition (CVD) using acetylene by employing 3D bicontinuous mesoporous silica (KIT-6) as a hard template, and used as the counter electrode in dye-sensitized solar cells (DSSCs). Here, we report that Ni-Cr-KIT-6 and Co-Cr-KIT-6 systems are most suitable catalysts for the growth of MWCNTs. Raman spectroscopy and TEM analysis revealed that the synthesized MWCNTs were of high quality and well-graphitized. Impressively, DSSCs with a MWCNT counter electrode demonstrated high power conversion efficiencies (PCEs) of up to 10.53%, which was significantly higher than that of 9.87% obtained for a DSSC with a

conventional Pt counter electrode. Moreover, MWCNTs had charge transfer resistance (R_{ct}) of only $0.74 \Omega \text{ cm}^2$ towards the I_3^-/I^- electrolyte commonly applied in DSSCs, which is several orders of magnitude lower than that of a typical Pt electrode ($2.78 \Omega \text{ cm}^2$). These results indicate that the synthesized MWCNT counter electrodes are versatile candidates that can increase the power conversion efficiency (PCE) of DSSCs.

KEYWORDS: Dye-sensitized solar cells, Efficiency, Electrochemical impedance spectroscopy, Multi-walled carbon nanotubes, Ni-Cr-KIT-6, Co-Cr-KIT-6

1. Introduction

Dye-sensitized solar cells (DSSCs) have attracted great interest as materials for third-generation photovoltaic devices because of their cost effective, high light-to-energy conversion efficiency, and high performance.¹⁻⁵ A classic DSSC consists of three key components: a dye-sensitized semiconductor photo anode, an electrolyte with a redox couple (tri-iodide/iodide (I_3^-/I^-)), and a counter electrode. The counter electrode is a vital constituent of DSSCs, where electrodes are injected into the electrolyte to catalyze the reduction of I_3^- .⁶ In DSSCs, a Pt counter electrode is the conventional electrode material used to encourage electrocatalytic activity for I_3^- reduction. However, Pt is expensive due to its scarcity, and DSSCs with a Pt counter electrode has poor thermal stability and weak corrosion resistance.⁷ To increase the electrical conductivity and electrocatalytic activity, we propose a novel method for the fabrication of Pt-free, cost effective, high power conversion efficiency (PCE) counter electrode materials for DSSCs.

Considerable efforts have been made to replace Pt with abundant cost effective alternatives, including fullerene,⁸ mesoporous carbon,⁹ activated carbon,¹⁰ molybdenum disulfide,¹¹ graphene,¹² and carbon nanotubes (CNTs).¹³ Among these counter electrode materials, high-quality CNTs possess high electrical conductivity and electrocatalytic activity for I_3^- reduction.¹⁴ Therefore, CNT based materials provide a suitable matrix for constructing a fast electron-transport network, and are popular electrode materials for various electronic devices because of their unique structure, remarkable electronic and electrocatalytic properties.^{15–20} Well-ordered CNTs with uniform diameter are of interest for the design of nanoelectronic devices such as fuel cells, supercapacitors, Li-ion batteries, sensors, nanorobots, and solar cells. Among the many methods available for the synthesis of CNTs, chemical vapour deposition (CVD) appears to be a promising and a viable method because of its cost effective to better control the structure when compared with other methods such as arc-discharge and laser ablation.²⁰ Fe, Co, Ni, Mo, and their alloys are used as catalysts, and Al_2O_3 , MgO, SiO_2 , $CaCO_3$, Zeolite, MCM-41, SBA-15, and KIT-6 are used as supports for CNT production.^{21,22} Yield and diameter of CNTs has been reported to vary according to the size of the transition metal particles on the surface of the support. The use of transition metal catalysts over an appropriate support is the preferred method for producing large amounts of CNTs at moderate temperatures.^{20,23}

Fine dispersed metal particles with nanometer sized catalysts are preserving their of morphology at the CVD synthesis processing temperature are essential since controlling the morphology of the catalyst particles during the CNTs synthesis strongly affects the CNTs shape, thickness, uniformity, quality and quantity. The size of the metal particles decreases to the nanometer size, they gradient to agglomerate. To avoid this, porous materials have been

anticipated as supports. For CNTs growth, the porous support exhibited a non-continuous surface and high surface area not only contribute significantly to the particle stabilization and produce the well-dispersed catalyst particles, but also drastically increase the number of the catalytic particles and nucleation sites, which are the advantageous for CNTs growth with high quality.¹⁶ To date, various nanomaterials such as 1D nanowires and 3D nanowire networks have been prepared using MCM-41 (p6mm), SBA-15 (p6mm), and KIT-6 (Ia3d) as hard templates.²⁴ Among them mesoporous materials, KIT-6 have an interesting three-dimensional (3D) cubic structure with interconnecting bi-continuous network channels, high thermal and hydrothermal stability.²⁵ Fascinatingly, mesoporous KIT-6 has tunable pore diameters between 4–11 nm, has a remarkable high surface area and pore volume, combined with a highly accessible and connected open porous networks. Mesoporous KIT-6 is therefore a useful hard template for the synthesis of various nanomaterials such as platinum nanorods, carbon nanorods (CNRs), and CNTs with a controlled diameter. Despite recent developments in soft and hard templates, however, the obtained morphologies of CNTs have been very limited; only powders with irregular morphology have been obtained. The lack of control over tube diameter and morphology is a serious obstacle to further development of CNTs. Shape and diameter are critical determinants of the functions and uses of CNTs. To obtain shape and diameter dependent physico-chemical properties, it is extremely important to prepare shape and diameter-controlled synthesis at high yields.

In this present investigation, we propose a new concept for the shape and diameter-controlled synthesis of multi-walled CNTs (MWCNTs) in hard templates. We demonstrate the facile synthesis of uniform diameter of MWCNTs by using mesoporous silica KIT-6 (Ia3d) as the hard

template. To the best of our knowledge, the high quality MWCNTs grown over bimetallic Ni-Cr-KIT-6 and Co-Cr-KIT-6 that we fabricated as cost-effective and Pt-free counter electrodes for use in DSSCs. DSSCs device with a counter electrode consisting of the synthesized MWCNTs exhibited a promising PCE of 10.53%, which is significantly higher than that obtained for a DSSC with a Pt counter electrode (9.87%). This results suggests that the DSSCs fabricated using MWCNTs (grown over bimetallic Ni-Cr-KIT-6 and Co-Cr-KIT-6) as a counter electrode which exhibited a superior performance than that of previous report ($< 8\%$).^{14,16,17,26} The R_{ct} values of the synthesized MWCNT electrodes were lower than that of the Pt counter electrode. Cyclic voltammetry measurements demonstrated that the electrocatalytic activities of the MWCNT-fabricated electrodes towards I_3^- reduction were higher than that of the Pt-fabricated electrode. DSSCs with synthesized MWCNTs also showed remarkable electrochemical stability of greater than 250 consecutive cycle scans. These results indicate that MWCNTs have tremendous promise for replacing Pt, which would substantially reduce the cost of DSSCs in future commercial applications.

2. Materials and Methods

2.1 Materials

Pluronic P123 triblock co-polymer [poly(ethylene glycol)-block-poly(propylene glycol)-block-poly(ethylene glycol)] with a molecular weight of 5800 ($EO_{20}PO_{70}EO_{20}$) and n-butanol (n-BuOH) purchased from Aldrich (Aldrich, UK) were used as the structure-directing agent and co-surfactant, respectively. Tetraethyl orthosilicate (TEOS) purchased from Aldrich was used as a silica source. Chromium nitrate, nickel nitrate, and cobalt nitrate were purchased from Aldrich and used as chromium, nickel, and cobalt sources, respectively. Ethanol, hydrochloric acid,

sodium hydroxide (NaOH), acetonitrile, and acetic acid were purchased from Merck. Chloroplatinic acid (H_2PtCl_6), iodide, lithium perchlorate, lithium iodide, 4-tert-butyl pyridine, 1,2-dimethyl-3-propylimidazolium iodide (DMPII), ethyl cellulose, and terpineol were purchased from Aldrich. The above chemicals were used without further purification. N719 dye [cis-di(thiocyanato)-n,n-bis(2,2'-bipyridyl-4-carboxylic acid-4-tetra butyl ammonium carboxylate) ruthenium (II)], fluorine-doped tin oxide (FTO) conducting glass plates (sheet resistance $13 \Omega \text{ sq}^{-1}$), and Surlyn 1702 were purchased from Solaronix SA, Switzerland.

2.2 Synthesis of metallic KIT-6 catalysts

Mesoporous monometallic Co-KIT-6 (Si/M ratios: 25, 50, 75 and 100), bimetallic Ni-Cr-KIT-6 (Si/M = 50), and Co-Cr-KIT-6 (Si/M = 50) catalysts were synthesized hydrothermally using a gel composition of TEOS: 0.017 P123: 1.83 HCl (35 wt. %): 1.31 n-BuOH: 195 H_2O .²⁷ The typical procedure for the synthesis of Cr-KIT-6 (25) was as follows: 4.0 g of P123 and 7.4 g of HCl (35 wt.%) were dissolved in 144 g of distilled water. To dissolve the template comprehensively, the above mixture was stirred for 3 h at 35 °C in distilled water and HCl. After complete dissolution, 4.0 g of n-BuOH was added to the above mixture, which was then stirred for another 30 min. TEOS (8.6 g) and the required amount of chromium source were added simultaneously to the above homogeneous solution. The mixture was stirred vigorously for 24 h at 35 °C and consequently transferred to a Teflon-lined stainless steel autoclave followed by aging at 100 °C for 48 h. Precipitated products were filtered without washing and dried at 80 °C for 10 h in atmospheric air. The dried as-synthesized mesoporous materials were ground well and then calcined at 540 °C for 5 h in a N_2 atmosphere followed by atmospheric air for 5 h to remove the template without any loss of mesoporous materials. This typical procedure was

adopted for the synthesis of Co-KIT-6 (Si/M ratios: 50, 75 and 100), Ni-Cr-KIT-6 (50), and Co-Cr-KIT-6 (50).

2.3 Synthesis of MWCNTs

MWCNTs were synthesized over Cr-KIT-6 (Si/M: 25, 50, 75 and 100), Ni-Cr-KIT-6 (50), and Co-Cr-KIT-6 (50) mesoporous catalysts. The CVD setup consists of a horizontal tubular furnace and gas flow control units. In a typical experiment, 200 mg of the catalyst was placed in a quartz boat inside the center of the quartz tube. The catalyst was purged using argon gas at a flow rate of 100 standard cubic centimeters per minute (sccm) for 30 min to remove water, and H₂ gas was purged at flow rate of 100 sccm for 30 min to reduce the metal particles. The reaction was carried out using acetylene at various temperatures (700–900 °C) at a flow rate of 50 sccm for 30 min. The furnace was then cooled to room temperature under an argon atmosphere. The % carbon deposition yield due to the catalytic decomposition of acetylene was calculated from the following equation:

$$\text{Carbon deposition yield (\%)} = \frac{m_{tot} - m_{cat}}{m_{cat}} \times 100 \quad (1)$$

where m_{tot} is the total mass of the carbon product with catalyst and m_{cat} is the mass of the catalyst only.

2.4 Purification of MWCNTs

The as-synthesized carbon black materials contained some impurities such as silica phase, metal particles, and carbonaceous impurities (e.g. amorphous carbon, microcrystalline carbon). A multi-step purification procedure was therefore adopted to purify the as-grown MWCNTs. The first step involved heating the as-synthesized carbon black materials in air at 450 °C for 1 h.

Then, the as-synthesized carbon black materials were sonicated in 6 M NaOH for 15 min and left to stand for 4 h.²⁸ NaOH treated materials were treated with hydrochloric acid (HCl) and nitric acid (HNO₃) to remove the metal particles and then washed with distilled water and dried at 100 °C for 6 h in atmospheric air. Finally, the materials were sintered at 450 °C in atmospheric air for 2 h in a muffle furnace to remove carbonaceous impurities.²⁹ Purified MWCNTs were characterized by scanning electron microscopy (SEM), transmission electron microscopy (TEM), Raman spectroscopy, thermogravimetric analysis (TGA &DTG), and X-ray diffraction (XRD).

2.5 Fabrication of TiO₂ working electrode and counter electrodes

The TiO₂ working electrode was fabricated as follows: FTO conducting glass substrates were ultrasonicated thoroughly in acetone, ethanol, and distilled water for 10 min to remove organic pollutants and other contaminants. 3.0 g of TiO₂ (P25 Degussa) powder was mixed with 0.5 mL of acetic acid and the mixture was sonicated for 30 min in an ultrasonic bath. 2.5 mL of water and 40 mL of ethanol were added to the above mixture followed by an additional 30 min of sonication. Terpineol and ethyl cellulose in ethanol were added to the above mixture. The above mixture was sonicated for 24 h to obtain a well-dispersed TiO₂ paste. This TiO₂ paste was coated over FTO by spin coating. After air drying, the TiO₂-coated FTO film was sintered at 500 °C for 1 h in a muffle furnace. TiO₂-coated FTO conducting substrate was immersed in 0.1 M HCl solution for 1 h and then washed with distilled water. The device was kept in TiCl₄ solution for 1 h, rinsed with distilled water, and then dried at room temperature. The fabricated TiO₂ thin film was dipped into a solution of N719 dye for 12 h in the dark at room temperature, rinsed with ethanol, and then dried and used as the working electrode (photo anode) in DSSCs.

Counter electrodes were fabricated as follows: MWCNT (grown over Ni-Cr-KIT-6 and Co-Cr-KIT-6) counter electrodes were prepared by spin coating. MWCNT paste was prepared by mixing 10–50 mg of synthesized MWCNTs with 10 mL of ethanol, to which 1 g of terpineol and 1 g of 5 wt.% ethyl cellulose in ethanol were added. The above mixture was sonicated for 30 min in an ultrasonic bath and ethanol was evaporated by incubating the mixture at 50 °C for 2 h. The paste was spin coated on FTO conducting substrate at 2000 rpm for 20 s and dried at 60 °C for 10 min in a vacuum. After drying, the MWCNT-coated FTO conducting substrate electrodes were heat-treated at 380 °C for 1 h in atmospheric air to increase the adhesion between MWCNTs and FTO conducting substrate. For comparison, a Pt electrode was prepared using a similar procedure. H_2PtCl_6 was dispersed in 10 mL of ethanol to which 1 g of terpineol and 1 g of 5 wt.% ethyl cellulose in ethanol were added. The mixture was ultrasonicated and dried to get a paste that was then coated on the FTO conducting substrate. The Pt-coated FTO conducting substrate was heat-treated at 400 °C for 1 h.

2.6 DSSC unit cell assembly

DSSCs were assembled by injecting the electrolyte into the aperture between the dye-sensitized TiO_2 working electrode and the MWCNT/Pt counter electrode. The liquid electrolyte was composed of 0.05 M I_2 , 0.1 M LiI, 0.6 M 1, 2-dimethyl-3-propylimidazolium iodide (DMPII), and 0.5 M 4-tert-butyl pyridine with acetonitrile as the solvent. Surlyn 1702 was used as a spacer between the two electrodes. The two electrodes were clipped together and solid paraffin was used as a sealant to prevent the electrolyte solution from leaking. The effective cell area was 0.25 cm^2 .

2.7 Characterization techniques

Samples for TEM analysis were prepared by initially dispersing the metallic 3D KIT-6 catalyst and MWCNTs in ethanol by ultra-sonication for 30 min, after which they were allowed to settle. A drop of the supernatant liquid was then transferred to a carbon-coated copper grid and mounted onto a transmission electron microscope (JEOL 3010) operated at 300 kV; micrographs were then recorded. Surface area, pore volume, and pore size distribution were measured by N₂ sorption at -197°C using an ASAP-2010 porosimeter from Micrometrics Corporation. Mesopore volume was estimated from the amount of N₂ adsorbed at a relative pressure of 0.5 assuming that all mesopores were filled with condensed nitrogen in the normal liquid state. Pore size distribution was estimated using the BJH algorithm (ASAP-2010) available as built-in software from Micrometrics. X-ray diffraction patterns of catalysts as well as CNTs were recorded with a PANalytical X'Pert diffractometer, using nickel-filtered CuK α radiation ($\lambda = 1.54 \text{ \AA}$) and a liquid nitrogen-cooled germanium solid-state detector. Diffractograms were recorded in the 2θ range of 0.5–10° for mesoporous metallic 3D KIT-6 catalysts and 10–80° for MWCNTs. Peaks were identified with reference to compilation of simulated XRD powder patterns. Amount of metal incorporated into the KIT-6 mesoporous catalyst was analyzed and determined by inductively coupled plasma-atomic emission spectroscopy (ICP-AES, Perkin Elmer OPTIMA 3000). Samples were dissolved in a mixture of HF and HNO₃ before the measurement. TGA measurements were carried out under atmospheric air using a high-resolution TA instrument (New Castle, DE, USA). About 20 mg of CNTs were used in each experiment. Samples were heated in air at a heating rate of 10 °C min⁻¹ in the temperature range from 40 to 1000 °C. Raman spectra were recorded between 500 and 2500 cm⁻¹ using a Nanofinder 30 confocal Raman

microscope (Tokyo Instruments Co., Japan), He–Ne laser beam with a wavelength of 488 nm, and charge-coupled device detector.

2.8 Electrochemical and photovoltaic measurements

Assembly and measurement of the electrochemical and photovoltaic properties of DSSCs were carried out as described below. Photovoltaic characteristics of the DSSCs were determined by measuring photocurrent density-cell voltage ($J-V$) using a Keithley 2000-semiconductor characterization system under simulated AM 1.5 solar illumination at 100 mW/cm^2 using a xenon arc lamp in ambient atmosphere. Intensity of light was measured with a radiant power/energy meter before each experiment. Electrochemical experiments were carried out using an electrochemical workstation (PGSTAT 30, Autolab, Eco-Chemie, Netherland). For electrochemical impedance spectroscopy (EIS) measurements, a thin layer symmetric cell was fabricated by clamping two identical MWCNT (grown over Ni-Cr-KIT-6 and Co-Cr-KIT6) or Pt-coated FTO electrodes to each other with Surlyn 1702 thermosetting polymer. EIS measurements were performed under normal conditions (without exposure to a light source) over a frequency range of 0.1 Hz to 100 KHz with perturbation amplitude of 10 mV. The space between electrodes was filled with the electrolyte, 0.05 M I_2 , 0.1 M LiI, 0.6 M 1,2-dimethyl-3-propylimidazolium iodide (DMPII), and 0.5 M 4-tert-butyl pyridine with acetonitrile through pre-drilled holes and sealed. Cyclic voltammograms (CVs) were recorded in acetonitrile solution containing 10 mM LiI + 1 mM I_2 + 0.1 M LiClO_4 using a three-electrode cell with Pt- or MWCNT (grown over Ni-Cr-KIT-6 and Co-Cr-KIT6)-coated FTO as the working electrode, a saturated calomel electrode as the reference electrode, and Pt wire as the counter electrode.

3. Results and Discussion

3.1 Morphology of the catalyst

The surface morphologies of Cr-KIT-6, Ni-Cr-KIT-6, and Co-Cr-KIT-6 were determined by SEM. Fig. S1 shows their spongy, and porous nature. The SEM study confirmed that the porous networks were not perturbed by metal loading.

HR-TEM images of Cr-KIT-6, Ni-Cr-KIT-6, and Co-Cr-KIT-6 revealed the presence of large domains of a 3D silica-metal network, highlighting the interconnectivity in pore structure of the Ia3d cubic phase (Fig. 1). HR-TEM images showed the representative morphology and distribution of Cr, Ni-Cr, and Co-Cr nanoparticles inside the pores of the 3D KIT-6 networks. A regular 3D pore structure with well-ordered arrays and metallic nanoparticles was present within the channels of the KIT-6 networks. Cr, Ni-Cr, and Co-Cr nanoparticles exhibited a narrow size distribution in the range of 3–5 nm. The distance between two consecutive centers of cubic pores estimated from the HR-TEM images was ca. 21 nm. No metal clusters were observed over the hydrothermally synthesized cubic mesoporous framework. Together, the TEM results revealed that metal nanoparticles were finely distributed in the 3D cubic KIT-6 framework.

3.2 Nitrogen adsorption-desorption isotherms of the catalysts

N₂ adsorption-desorption isotherms of Cr-KIT-6, Ni-Cr-KIT-6, and Co-Cr-KIT-6 are shown in Fig. 2. Calculated surface area, pore size, and pore volume of Cr-KIT-6, Ni-Cr-KIT-6, and Co-Cr-KIT-6 are tabulated in Table S1. Isotherms were type 1V isotherms with a pronounced capillary condensation step, characteristic of high-quality large pore mesoporous materials. Pore size distributions of Cr-KIT-6, Ni-Cr-KIT-6, and Co-Cr-KIT-6 were calculated by the BJH method. The presence of a H1 hysteresis loop revealed that all materials had good structural

ordering of the mesoporous network with a relatively narrow pore size distribution. Sharp steps observed at the relative partial pressure range of 0.6–0.8 corresponded to capillary condensation of N₂ and indicated the uniformity of the pores. Maximum surface area of the synthesized metallic KIT-6 materials was in the range of 789–796 m²/g based on BET studies. This result confirmed that all synthesized mesoporous network had a high surface area, uniform pore size, and well-ordered structure. This was further confirmed by the observation that ordering of the cubic arrays of the mesopores in KIT-6 was barely affected by incorporation of a high metal content, as observed from the small-angle XRD findings (Fig. S2).

3.3 XRD pattern of the catalysts

Small-angle XRD patterns of calcined monometallic Cr-KIT-6, bimetallic Ni-Cr-KIT-6, and Co-Cr-KIT-6 are shown in Fig. S2. A high intensity peak in the 2θ range of 0.7–0.9° due to the (211) diffraction line and a shoulder around $2\theta = 1.0$ –1.1° due to the (200) diffraction line were observed. This pattern revealed excellent structural order with symmetry commensurate to a body-centered cubic Ia3d space group, consistent with previously published data.³⁰ The XRD pattern of the calcined materials confirmed that there was no structural deformation or change in phase during calcination. These results suggested that metallic 3D KIT-6 had excellent thermal stability and structural uniformity after calcination at a high temperature. The cubic nature of the host KIT-6 was not affected by incorporating metal nanoparticles at maximum loading.

Fig. S3 shows the wide-angle XRD patterns of Cr-KIT-6, Ni-Cr-KIT-6, and Co-Cr-KIT-6 mesoporous materials. In the wide-angle region, calcined materials showed a broad diffraction peak at 2θ around 15–35°, corresponding to amorphous silica walls of the 3D cubic mesoporous materials. However, no crystalline phase (or) agglomerated particles appeared with a high

loading of metal. This suggested that the metal nanoparticles were uniformly dispersed within the KIT-6 silica matrix; no metal particles were observed on the silica framework. This is consistent with the HR-TEM results that showed that all metal ions were uniformly dispersed in the mesoporous KIT-6 materials.

Together, the TEM results, N₂ adsorption-desorption isotherm results, and small-angle XRD patterns confirmed that the method employed in this study was suitable to obtain mesoporous silica with highly ordered 3D KIT-6 cubic networks.

3.4 Elemental analysis of the catalysts

Metal composition of hydrothermally synthesized mono- and bimetallic KIT-6 were analyzed by ICP-AES. Si/M ratio of calcined monometallic Cr-KIT-6, bimetallic Ni-Cr-KIT-6, and Co-Cr-KIT-6 materials were calculated and are shown in Table S1. Si/M ratio derived by elemental analysis was very similar to that of the gel composition, as has been observed previously for mesoporous materials.³⁰ The results proved that all mono- and bimetallic systems employed during synthesis were successfully incorporated into the 3D KIT-6 cubic network. We expected this to enhance the interaction between metal and silica phases.

3.5 FT-IR spectroscopy of the catalysts

FT-IR spectra of as-synthesized and calcined mesoporous materials (Cr-KIT-6, Ni-Cr-KIT-6, and Co-Cr-KIT-6) are shown in Figs. S4 (a) and (b), respectively, and described in detail in the supporting information.

3.6 Optimization conditions for synthesis of high quality MWCNTs at high yields

Catalytic material activities were evaluated to synthesize MWCNTs by CVD. MWCNTs were synthesized over monometallic (Cr-KIT-6 (Si/M = 25, 50, 75 and 100) catalyst at 800 °C and the results are summarized in Table S2. The highest carbon deposition was achieved in Cr-KIT-6 (50). Higher loading of metals resulted in irregular dispersion and the formation of bulk and clustered metallic particles. This decreased the number of active sites and surface area, thereby affecting the growth of MWCNTs. Efficiency of optimized Cr-KIT-6 (50) for the synthesis of MWCNTs at different temperatures (700–900 °C) was studied. Maximum carbon deposition yield was obtained at 800 °C, followed by 900 and 700 °C (Fig. S5). In this experiment, we varied the ratio of Ni: Cr and Co: Cr (1:1, 1:2, 1:3, 3:1, 2:1) when synthesizing MWCNTs. However, Ni: Cr and Co: Cr ratios of 1:1 displayed the best properties when compared to the other metal ratios. Carbon deposition yield was as follows: Ni-Cr-KIT-6 > Co-Cr-KIT-6 > Co-KIT-6 (50) at the reaction temperature of 800 °C.

Fig. S5 shows the effect of reaction temperature on carbon deposition yield over Cr-KIT-6, Ni-Cr-KIT-6, and Co-Cr-KIT-6 catalysts for 30 min. The experiment was carried out at temperatures ranging from 700–900 °C at intervals of 100 °C under the conditions of a constant growth time of 30 min and an acetylene flow rate of 50 sccm. As temperature increased, carbon deposition yield increased rapidly, and reached $\geq 424\%$ at 800 °C. Nanotubes that formed at the lower growth temperature of 700 °C were less dense than those that formed at higher temperatures, perhaps due to an insufficient amount of metal nanoparticles. MWCNTs formed at 800 °C were of uniform diameter and had a higher density and yield than those obtained at 700 and 900 °C. Therefore, the decomposition rate of acetylene and the deposition rate of carbon

atoms on metal nanoparticles reached a balance at 800 °C. The above results clearly indicated that metal nanoparticles were incorporated into the 3D KIT-6 network, resulting in high quality MWCNTs. At 900 °C, carbonaceous impurities, such as amorphous carbon and microcrystalline carbon, were observed.

The flow rate of the carbon precursor (acetylene) plays an energetic role in determining the carbon deposition yield and quality of MWCNTs. We therefore maintained the reaction temperature and time at the optimized conditions of 800 °C and 30 min, respectively, while varying the acetylene flow rate (10–80 sccm). Optimal flow rate was 50 sccm/min with a carbon deposition yield of 426% MWCNTs with minimal impurities. Amorphous carbon and other carbonaceous impurities do not form at low concentrations of carbon precursor (i.e. 10–40 sccm); a very small amount of carbonaceous impurities was observed because some metal particles were not bound to the KIT-6 framework. The amount of carbonaceous impurities increased when the flow rate of acetylene was increased above 50 sccm (i.e. 60 sccm and more).

3.7 Morphological study of MWCNTs

The insight morphology of MWCNTs was analyzed by TEM. TEM images and selected area electron diffraction (SAED) patterns of MWCNTs (grown over Ni-Cr-KIT-6 and Co-Cr-KIT-6) are shown in Fig. 3. MWCNTs comprised 12–16 graphene sheets with a graphene layer thickness of around 0.34–0.35 nm. Diameters of MWCNTs were about 17–19 nm and 14–16 nm for growth over Ni-Cr-KIT-6 and Co-Cr-KIT-6, respectively. Due to the higher decomposition rate of acetylene precursors into Ni-Cr-KIT-6 catalyst produced MWCNTs slightly higher thickness than that of Co-Cr-KIT-6 catalytic system. This result suggests that Ni containing Cr-KIT-6 active in acetylene than Co containing Cr-KIT-6. Highly dense, rope-like carbon

nanostructures grew from the surface of the KIT-6 support; higher magnification revealed that these nanostructures had a hollow core structure. Moreover, the observed MWCNTs were of more uniform diameter and higher quality than commercial MWCNTs (results not shown). Both catalysts (Ni-Cr-KIT-6 and Co-Cr-KIT-6) produced MWCNTs with comparable morphology at high yield. TEM analysis revealed the absence of carbonaceous impurities on the surfaces of the MWCNTs. These results suggested that use of Ni-Cr-KIT-6 and Co-Cr-KIT-6 as mesoporous catalytic materials resulted in high quality MWCNTs with a uniform diameter. The narrow inner and outer diameters and high purity of synthesized MWCNTs suggested that these MWCNTs could display enhanced electrical conductivity and electrocatalytic activity.

3.8 Raman spectroscopy analysis of MWCNTs

Raman spectroscopy is a powerful tool for the characterization of CNTs. Carbon allotropes including fullerene, graphite, amorphous carbon, CNTs, and graphene are active in Raman spectroscopy. However, the position, width, and relative intensity of bands are modified according to the carbon allotrope.³¹ Fig. 4 shows the Raman spectra of MWCNTs (grown over Ni-Cr-KIT-6 and Co-Cr-KIT-6). Two major peaks around 1335–1345 cm^{-1} and 1578–1581 cm^{-1} , corresponding to D and G-bands, respectively, were observed. The G-band indicates formation of a well-ordered hexagonal lattice of graphite, whereas the D-band indicates the formation of disorder in the lattice of graphite. The peak intensities of the G- and D-bands are denoted I_G and I_D , respectively. In the obtained spectra, the G-band was of higher intensity than the D-band, therefore the MWCNTs had $I_G/I_D > 1$, indicating that the bimetallic KIT-6 (Ni-Cr-KIT-6 and Co-Cr-KIT-6)-produced MWCNTs were of high quality and well-graphitized structure. Furthermore, only two Raman bands appeared in the high wave number region, indicating that

the synthesized CNTs were most likely MWCNTs. The absence of radial breathing mode (RBM) in the lower wave number region (below 500 cm^{-1}) confirmed that the synthesized CNTs were MWCNTs.

3.9 Thermogravimetric analysis of MWCNTs

Fig. S6 shows TGA and DTG results for the MWCNTs (grown over Ni-Cr-KIT-6 and Co-Cr-KIT-6). Both samples displayed similar weight loss characteristic properties. Weight loss in the temperature range between 560 and $640\text{ }^{\circ}\text{C}$ was attributed to the oxidation of MWCNTs. There was no weight loss below $560\text{ }^{\circ}\text{C}$, indicating the absence of carbonaceous impurities (amorphous carbon and microcrystalline carbon), because the combustion of amorphous carbon occurs below $400\text{ }^{\circ}\text{C}$. Moreover, no weight loss was observed beyond $640\text{ }^{\circ}\text{C}$; this proved that the MWCNTs were of high quality without impurities such as metallic particles or silica phases. The TGA study revealed that the synthesized MWCNTs had high thermal stability due to the presence of well-graphitized graphene walls.

3.10 XRD patterns of MWCNTs

Fig. S7 shows the XRD pattern of pure MWCNTs (grown over Ni-Cr-KIT-6 and Co-Cr-KIT-6). Strong peaks at $2\theta = 24.98\text{--}25.25^{\circ}$ and weak peaks at $2\theta = 43.62\text{--}44.34^{\circ}$ were observed, which we assigned to the (002) and (100) diffraction patterns of typical graphite, respectively. These XRD patterns indicated the absence of carbonaceous impurities and metal nanoparticles in the synthesized MWCNTs. In other words, the MWCNTs were well-graphitized and free from impurities (metal nanoparticles and carbonaceous impurities).³² Based on the TEM, Raman

spectroscopy, TGA, and XRD, we concluded that the synthesized MWCNTs were suitable materials for electronic applications.

3.11 Photocurrent density–cell voltage (J – V) characterization

Photovoltaic parameters of DSSCs fabricated using MWCNTs (grown over Ni-Cr-KIT-6 and Co-Cr-KIT-6) and Pt are shown in Table 1, and corresponding J – V characteristic curves are shown in Fig. 5. Fill factor (FF) and overall light-to-electrical energy conversion efficiency (η) were calculated as follows (Equations 2 and 3):

$$FF = \frac{I_{max} V_{max}}{I_{sc} V_{oc}} \quad (or) \quad FF = \frac{J_{max} V_{max}}{J_{sc} V_{oc}} \quad (2)$$

$$\eta (\%) = \frac{J_{max} V_{max}}{P_{in}} \times 100 \quad (or) \quad \eta (\%) = \frac{FF J_{sc} V_{oc}}{P_{in}} \times 100 \quad (3)$$

J_{sc} is the short circuit current density (mA/cm²), V_{oc} is the open circuit voltage (V), P_{in} is the incident light power (mA/cm²), and J_{max} and V_{max} are the current density and voltage at the point maximum of power output of the J – V (I – V) curves, respectively. For the cell built with a Pt counter electrode with an active area of 0.25 cm², $V_{oc} = 0.80$ V, FF = 75.8%, and $\eta = 9.87\%$. For MWCNTs (grown over Ni-Cr-KIT-6), $V_{oc} = 0.79$ V, FF = 75.7%, and $\eta = 10.53\%$, respectively. MWCNTs (grown over Co-Cr-KIT-6) had V_{oc} , FF, and η values of 0.78 V, 75.9%, and 10.44%, respectively. The increasing the photovoltaic (solar cells) parameters for the MWCNTs (grown over Ni-Cr-KIT-6) could be attributed to the presence of more active catalytic sites in the multilayer CNTs structure. These results indicate that MWCNTs (grown over Ni-Cr-KIT-6) have higher PCE than that of MWCNTs (grown over Co-Cr-KIT-6) due to the increase in the thickness of MWCNTs (more concentric graphene layer) which enhance the electrocatalytic

activity and electron-transport kinetics. Hence, the MWCNTs grown over Ni-Cr-KIT-6 (10.53%) have slightly higher efficiency than that of Co-Cr-KIT-6 grown MWCNTs (10.44%).¹³ The DSSCs with MWCNTs counter electrode possess a catalytically active to guarantee a promptly efficient reduction of I_3^- to I^- .

In previous study, DSSCs fabricated with MWCNTs as a counter electrode exhibited a PCE of < 8%, which is comparable to that of Pt based DSSCs (\approx 8.30%).¹⁷ The reported PCEs of DSSCs fabricated with MWCNTs and hybrid electrodes are shown in Table 2; the PCEs range from 4.02 to 9.05%. The differences in PCEs of MWCNTs and different carbon-based counter electrodes is mainly due to the use of different synthesis techniques for MWCNTs and differences in carbon-based material fabrication of DSSCs.³³⁻⁴⁷ These results suggest that uniform diameter, defect-free and high quality of MWCNTs (synthesized over bimetallic Ni-Cr-KIT-6 and Co-Cr-KIT-6) in the present investigation is the cause for the enhancement of the PCE (>10%) than the previous reports.^{14,16,17,26} The PCEs of our MWCNT counter electrode-based cells are slightly higher than those of Pt-based DSSCs. The PCE of MWCNT-based DSSCs can be further improved by enhancing the FF, increasing the purity of the materials, and/or optimizing device architecture to enhance light absorption and facilitate electron transport.

3.12 Electrochemical impedance spectroscopy (EIS) analysis

To further elucidate the electrochemical characteristics of Pt and MWCNT (grown over Ni-Cr-KIT-6 and Co-Cr-KIT-6) electrodes, EIS measurements were performed on dummy cells with a symmetric sandwich-like structure - counter electrode/electrolyte/counter electrode. Fig. 6 shows Nyquist plots of Pt and MWCNTs (grown over Ni-Cr-KIT-6 and Co-Cr-KIT-6). High frequency

(corresponding to low Z') intercept on the real axis (Z' axis) represents the series resistance R_s . The semicircle in the high-frequency range results from charge-transfer resistance (R_{ct}) and the corresponding constant phase-angle element (CPE) at the electrolyte/counter electrode interface.^{48,49} The semicircle in the low-frequency range (corresponding to a high Z') arises from Nernst diffusion impedance of the I_3^-/Γ^- couple of the electrolyte.⁴⁹

Values of R_{ct} obtained by fitting the spectra in Fig. 6 with an EIS spectra analyzer are summarized in Table 1. R_{ct} values of MWCNT (grown over Ni-Cr-KIT-6 and Co-Cr-KIT-6) counter electrodes were lower than those of Pt. The R_{ct} for I_3^-/Γ^- redox reaction is lower on the MWCNTs electrode compared with the Pt electrode under the same conditions. The low R_{ct} of the MWCNTs indicates that they have superior electrocatalytic activity and a larger surface area than Pt.⁴⁹ The EIS results agreed well with the $J-V$ experimental results. Therefore, the PCEs of the DSSCs with the counter electrode fabricated from MWCNTs was higher than that of Pt counter electrode as shown in previous report.⁵⁰

3.13 Cyclic voltammetric (CV) analysis

To investigate the conditions of the redox reaction of Γ^- ions at the counter electrode of the DSSCs, electrolyte solution containing I_3^-/Γ^- was used in the cyclic voltammetric (CV) measurements. Fig. 7 shows that the CVs of Pt and MWCNT (grown over Ni-Cr-KIT-6 and Co-Cr-KIT-6) electrodes at the scan rate of 25 mV/s. All pairs of redox peaks (anodic and cathodic peaks) were obtained for all counter electrodes according to equations 4 and 5:⁵¹



The CV studies shows a much larger current density of I_3^- reduction peak for MWCNTs than that of Pt electrode this suggests a faster reaction rate on the MWCNTs electrode than that of the Pt electrode. Due to the large surface area and more conducting channels of the MWCNTs modified electrode compared to Pt electrode MWCNTs act as an electrocatalyst and increase the current density and decrease the cathodic overpotential. This indicates that the MWCNT electrodes had superior conductivity and electrocatalytic activity to the Pt electrode.

Fig. S8 shows 250 continuous cycle scans of MWCNT (grown over Ni-Cr-KIT-6 and Co-Cr-KIT-6) counter electrodes (scan rate: 25 mV/s). CV curves scarcely changed and maximum redox peak current density showed an enhanced curve shape and constant redox peak current density, indicating that the MWCNT counter electrodes excellent electrochemical stability. The CV study revealed the maximum peak current density of the MWCNT electrodes and indicated that they had greater stability than the Pt electrode, which we attributed to the FTO conducting substrate.

4. Conclusions

We developed an environmentally friendly, and safe synthesis method to create highly efficient MWCNT-based electrocatalysts for high-performance DSSCs. High quality and well-graphitized MWCNTs were successfully synthesized over Ni-Cr-KIT-6 and Co-Cr-KIT-6-ordered mesoporous networks. These catalysts produced high density, high purity MWCNTs with a diameter of 14–19 nm. Optimized reaction conditions for the formation of high quality MWCNTs with high yield were 50 sccm/min of acetylene at a temperature of 800 °C for 30 min. Mesoporous Ni-Cr-KIT-6 and Co-Cr-KIT-6 molecular sieves exhibited good structural stability and are promising catalysts for large-scale growth of MWCNTs. TEM and Raman spectroscopic

studies confirmed the presence of high quality MWCNTs that were relatively defect-free with minimal carbonaceous impurities. This method represents a generic platform for the preparation of MWCNTs that can be used for other nanomaterials. Well-defined morphology and size uniformity are very important aspects of MWCNTs used in a wide range of applications such as Li-ion batteries, supercapacitors, solar cells, sensors, and drug delivery.

Compared with Pt, these MWCNTs exhibited excellent electrocatalytic activity towards I_3^-/I^- redox reactions due to their graphitization, defect-free nature, high surface area, and remarkable stability, which resulted in an enhanced electron transfer rate and faster ion transfer kinetics. Replacement of the precious metal Pt with cost effective counter electrode materials obtained by facile synthesis of MWCNTs will decrease the cost of DSSCs. These results have tremendous implications for future development of cost effective MWCNT-based electrocatalytic materials.

Acknowledgements

J. Balamurugan acknowledges support from the Converging Research Center Program (2014M3C1A8048834) and the Basic Research Laboratory Program (2014R1A4A1008140) through the Ministry of Science, ICT & Future Planning and the Basic Science Research Program through the National Research Foundation (NRF) funded by the Ministry of Education of Korea (2013R1A1A2011608).

Notes and References

- 1 M. Gratzel, *Nature*, 2010, **414**, 338–344.
- 2 A. I. Hochbaum and P. Yang, *Chem. Rev.*, 2010, **110**, 527–546.
- 3 B. E. Hardin, H. J. Snaith, M. D. Mc Gehee, *Nat. Photonics*, 2012, **6**, 162–169.
- 4 T. W. Hamann, R. A. Jensen, A. B. F. Martison, H. V. Ryswkac and J. T. Hup, *Energy Environ. Sci.*, 2008, **1**, 66–78.
- 5 L. M. Peter, *Phys. Chem. Chem. Phys.*, 2007, **9**, 2630–2642.
- 6 H. G. Boschloo and A. Hagfeldt, *Acc. Chem. Res.*, 2009, **42**, 1819–1826.
- 7 Y. C. Wang, D. Y. Wang, Y. T. Jiang, H. A. Chen, C. C. Chen, K. C. Ho, H. L. Chou and C. W. Chen, *Angew. Chem. Int. Ed.*, 2013, **52**, 6694–6698.
- 8 T. Hino, Y. Ogawa and N. Kuramoto, *Carbon*, 2006, **44**, 880–887.
- 9 G. Q. Wang, W. Xing and S. P. Zhuo, *J. Power sources*, 2009, **194**, 568–573.
- 10 J. K. Chen, K. X. Li, Y. H. Luo, X. Z. Guo, D. M. Li, M. H. Deng, S. Q. Huang and Q. B. Meng, *Carbon*, 2009, **47**, 2704–2708.
- 11 J. Zhang, S. Najmaei, H. Lin and J. Lou, *Nanoscale*, 2004, **6**, 5279–5283.
- 12 D. W. Zhang, X. D. Li, H. B. Li, S. Chen, Z. Sun, X. J. Yin and S. M. Huang, *Carbon*, 2011, **49**, 5382–5388.
- 13 S. U. Lee, W. S. Choi and B. Y. Hong, *Sol. Energy Mater. Sol. Cells*, 2010, **94**, 680–685.
- 14 W. J. Lee, E. Ramasamy, D. Y. Lee and J. S. Song, *ACS Appl. Mater. Interfaces*, 2009, **1**, 1145–1149.
- 15 S. Cataldo, P. Salice, E. Menna and B. Pignataro, *Energy Environ. Sci.*, 2012, **5**, 5919–5940.
- 16 Z. Yang, T. Chen, R. He, G. Guan, H. Li, L. Qiu and H. Peng, *Adv. Mater.*, 2011, **23**, 5436–5439.
- 17 Z. Fan, J. Yan, L. Zhi, Q. Zhang, T. Wei, J. Feng, M. Zhang, W. Qian and F. Wei, *Adv. Mater.*, 2010, **22**, 3723–3728.
- 18 J. Svensson, N. Lindahl, H. Yun, M. Seo, D. Midtvedt, Y. Tarakanov, N. Lindvall, O. Nerushev, J. Kinaret, S. Lee and E. E. B. Campbell, *Nano Lett.*, 2011, **11**, 3569–3575.
- 19 K. H. An, S. Y. Jeong, H. R. Hwang and Y. H. Lee, *Adv. Mater.*, 2004, **16**, 1005–1009.

- 20 G. D. Nessim, *Nanoscale*, 2010, **2**, 1306–1323.
- 21 J. Prasek, J. Drbohlavova, J. Chomoucka, J. Hubalek, O. Jasek, V. Adam and R. Kizek, *J. Mater. Chem.*, 2011, **21**, 15872–15884.
- 22 M. E. Davis, *Nature*, 2002, **417**, 813–821.
- 23 C. Ducati, I. Alexandrou, M. Chhowalla, G. A. J. Amaratunga and J. Robertson, *J. Appl. Phys.*, 2002, **92**, 3299–3303.
- 24 H. Wang, H. Y. Jeong, M. Imura, L. Wang, L. Radhakrishnan, N. Fujita, T. Castle, O. Terasaki and Y. Yamauchi, *J. Am. Chem. Soc.*, 2011, **133**, 14526–14529.
- 25 B. Hu, H. Liu, K. Tao, C. Xiong and S. Zhou, *J. Phys. Chem. C*, 2013, **117**, 26385–26395.
- 26 E. Ramasamy, W. J. Lee, D. Y. Lee and J. S. Song, *Electrochem. Commun.*, 2008, **10**, 1087–1089.
- 27 F. Kleitz, S. H. Choi and R. Ryoo, *Chem. Commun.*, 2003, **21**, 2136–2137.
- 28 S. Okubo, T. Sekine, S. Suzuki, Y. Achiba, K. Tsukagoshi, Y. Aoyagi and H. Kataura, *Jap. J. Appl. Phys.*, 2004, **43**, L396–L398.
- 29 A. Chenite, Y. Lepage and A. Sayari, *Chem. Mater.*, 1995, **7**, 1015–1019.
- 30 X. Sun, Y. Shi, P. Zhang, C. Zheng, X. Zheng, F. Zhang, Y. Zhang, N. Guan, D. Zhao and G. D. Stucky, *J. Am. Chem. Soc.*, 2011, **133**, 14542–14545.
- 31 R. Saito, M. Hofmann, G. Dresselhaus, A. Jorio and M. S. Dresselhaus, *Adv. Phys.*, 2011, **60**, 413–550.
- 32 J. C. Juan, Y. Jiang, X. Meng, W. Cao, M. A. Yarmo and J. C. Zhang, *Mater. Res. Bull.*, 2007, **42**, 1278–1285.
- 33 M. Wu, X. Lin, A. Hagfeldt and T. Ma, *Angew. Chem.*, 2011, **123**, 3582–3586.
- 34 M. Wu, X. Lin, A. Hagfeldt and T. Ma, *Angew. Chem. Int. Ed.*, 2011, **50**, 3520–3524.
- 35 Z. Huang, X. Liu, K. Li, D. Li, D. Li, Y. Luo, H. Li, W. Song, L. Chen and Q. Meng, *Electrochem. Commun.*, 2007, **9**, 596–598.
- 36 S. Huang, Z. Yang, L. Zhang, R. He, T. Chen, Z. Cai, Y. Luo, H. Lin, H. Cao, X. Zhu and H. Peng, *J. Mater. Chem.*, 2012, **22**, 16833–16838.
- 37 M. H. Yeh, L. Y. Lin, C. L. Sun, Y. A. Leu, J. T. Tsai, C. Y. Yeh, R. Vittal and K. C. Ho, *J. Phys. Chem. C*, 2014, **118**, 16626–16634.

- 38 P. Joshi, L. Zhang, Q. Chen, D. Galipeau, H. Fong and Q. Qiao, *ACS Appl. Mater. Interfaces*, 2010, **2**, 3572–3577.
- 39 G. R. Li, F. Wang, Q. W. Jiang, X. P. Gao, and P. W. Shen, *Angew. Chem. Int. Ed.*, 2010, **49**, 3653–3656.
- 40 Y. Xiao, J. Wu, J. Lin, G. Yue, J. Lin, M. Huang, Y. Huang, Z. Lana and L. Fan, *J. Mater. Chem. A*, 2013, **1**, 13885–13889.
- 41 F. Malara, M. Manca, M. Lanza, C. Hubner, E. Piperopoulou and G. Gigli, *Energy Environ. Sci.*, 2012, **5**, 8377–8383.
- 42 X. H. Yang, J. W. Guo, S. Yang, Y. Hou, B. Zhang and H. G. Yang, *J. Mater. Chem. A*, 2014, **2**, 614–619.
- 43 K. S. Lee, W. J. Lee, N. G. Park, S. O. Kim and J. H. Park, *Chem. Commun.*, 2011, **47**, 4264–4266.
- 44 S. Y. Tai, C. J. Liu, S. W. Chou, F. S. S. Chien, J. Y. Lin and T. W. Lin, *J. Mater. Chem.*, 2012, **22**, 24753–24759.
- 45 C. Y. Neo and J. Ouyang, *J. Mater. Chem. A*, 2013, **1**, 14392–14401.
- 46 S. Roy, R. Bajpai, A. K. Jena, P. Kumar, N. kulshrestha and D. S. Misra, *Energy Environ. Sci.*, 2012, **5**, 7001–7006.
- 47 Z. Yang, M. Liu, C. Zhang, W. W. Tjiu, T. Liu and H. Peng, *Angew. Chem. Int. Ed.*, 2013, **52**, 3996–3999.
- 48 S. Li, Y. Luo, W. Lv, W. Yu, S. Wu, P. Hou, Q. Yang, Q. Meng, C. Liu and H. M. Cheng, *Adv. Energy Mater.*, 2011, **1**, 486–490.
- 49 F. Hao, P. Dong, J. Zhang, Y. Zhang, P. E. Loya, R. H. Hauge, J. Li, J. Lou and H. Lin, *Sci. Rep.*, 2012, **2**, 1–6.
- 50 K. Imoto, K. Takahashi, T. Yamaguchi, T. Komura, J. Nakamura and K. Murata, *Sol. Energ. Mater. Sol. Cells*, 2003, **79**, 459–469.
- 51 P. Joshi, Z. Zhou, P. Poudel, A. Thapa, X. F. Wu and Q. Qiao, *Nanoscale*, 2012, **4**, 5659–5664.

Figure captions

Fig. 1 HR-TEM images of (a) Cr-KIT-6, (b) Ni-Cr-KIT-6, and (c) Co-Cr-KIT-6 mesoporous catalysts.

Fig. 2 N₂ adsorption-desorption isotherms of (a) Cr-KIT-6, (b) Ni-Cr-KIT-6, and (c) Co-Cr-KIT-6 mesoporous catalysts.

Fig. 3 TEM and SAED pattern of MWCNT grown over: (a–d) Ni-Cr-KIT-6 and (e–h) Co-Cr-KIT-6.

Fig. 4 Raman spectra of (a) MWCNTs (grown over Ni-Cr-KIT-6) and (b) MWCNTs (grown over Co-Cr-KIT-6).

Fig. 5 Photocurrent density–cell voltage (J – V) performance of (a) Pt Vs MWCNT- (grown over Ni-Cr-KIT-6) and (b) Pt Vs MWCNT (grown over Co-Cr-KIT-6) counter electrode DSSCs at 100 mW/cm² of simulated solar illumination.

Fig. 6 Electrochemical impedance spectra of (a) Pt Vs MWCNTs (grown over Ni-Cr-KIT-6) and (b) Pt Vs MWCNTs (grown over Co-Cr-KIT-6).

Fig. 7 Cyclic voltammograms of (a) Pt Vs MWCNT (grown over Ni-Cr-KIT-6) and (b) Pt Vs MWCNT (grown over Co-Cr-KIT-6) electrodes in acetonitrile solution containing 10 mM LiI + 1 mM I₂ + 0.1 M LiClO₄ at a scan rate of 25 mV/s.

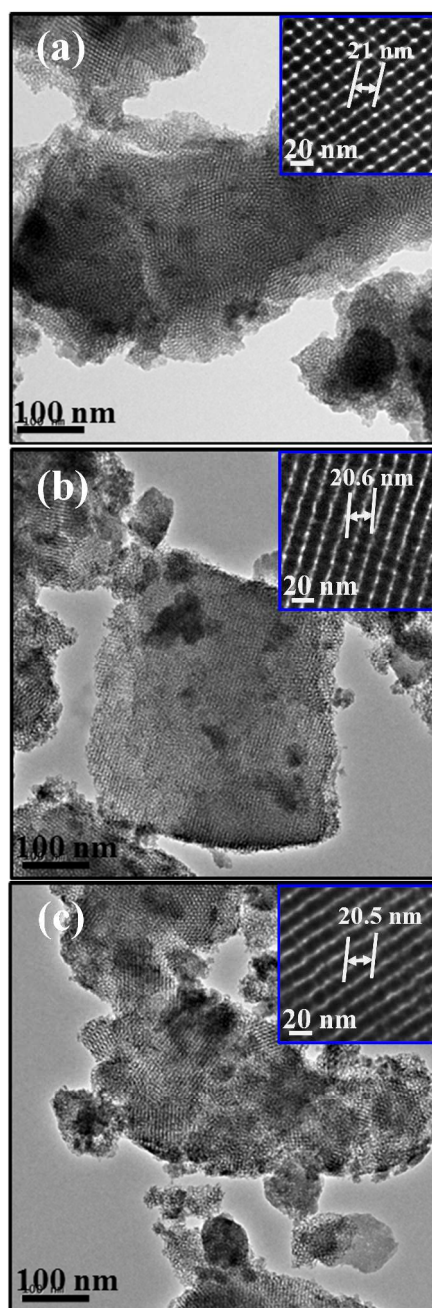


Fig. 1 HR-TEM images of (a) Cr-KIT-6, (b) Ni-Cr-KIT-6, and (c) Co-Cr-KIT-6 mesoporous catalysts.

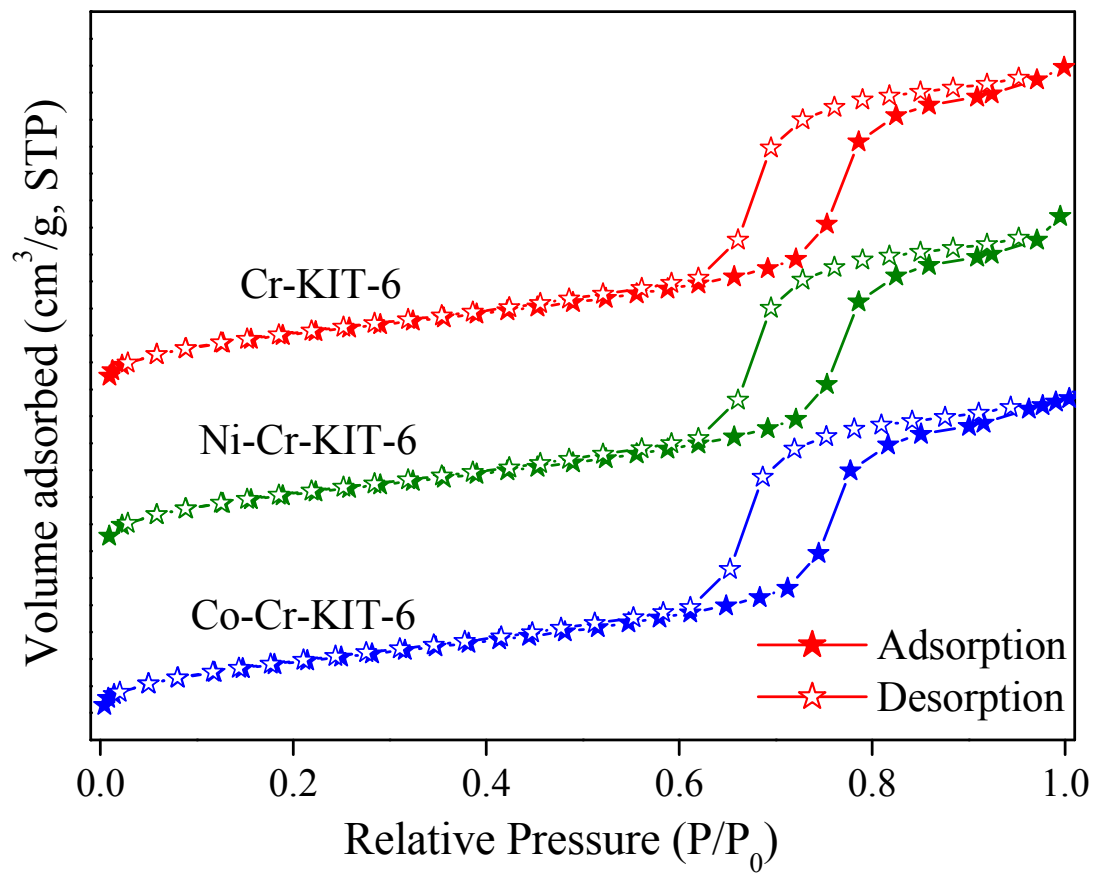


Fig. 2 N₂ adsorption-desorption isotherms of (a) Cr-KIT-6, (b) Ni-Cr-KIT-6, and (c) Co-Cr-KIT-6 mesoporous catalysts.

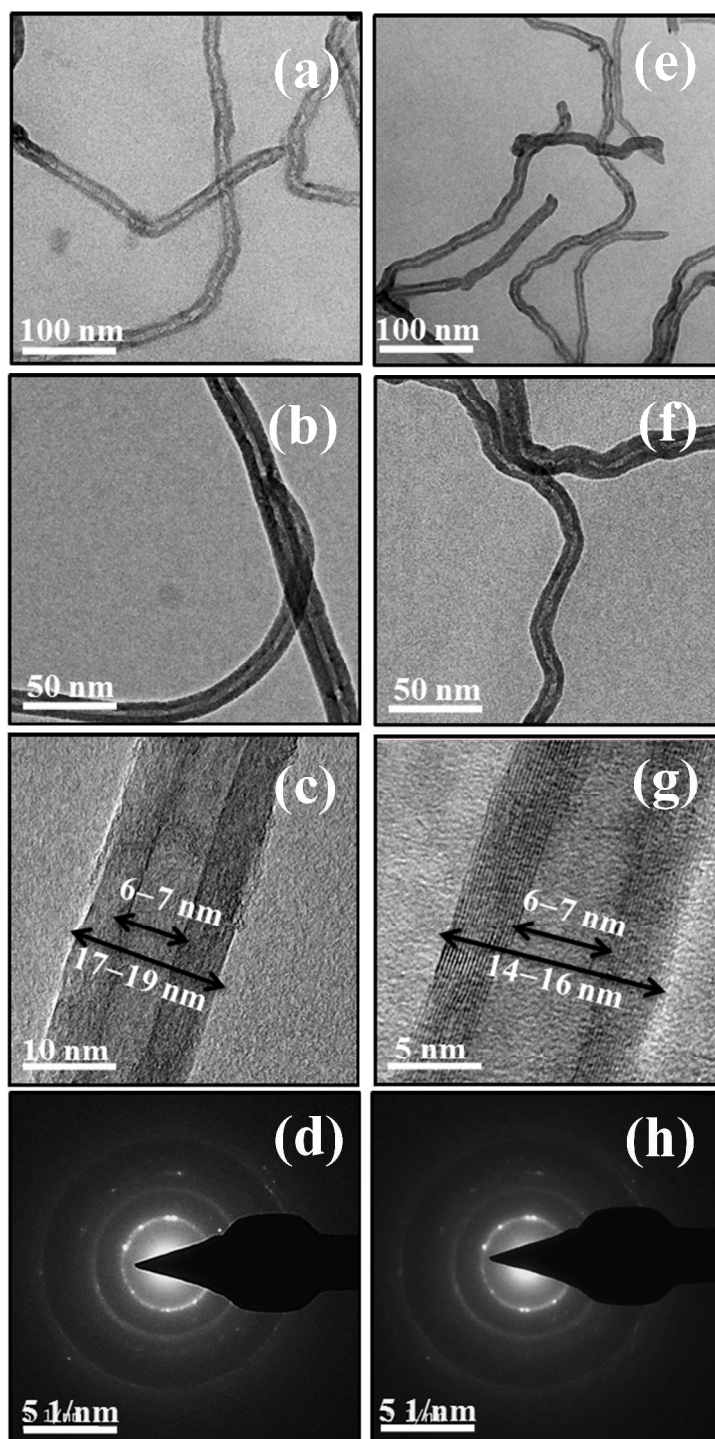


Fig. 3 TEM and SAED pattern of MWCNT grown over: (a-d) Ni-Cr-KIT-6 and (e-h) Co-Cr-KIT-6.

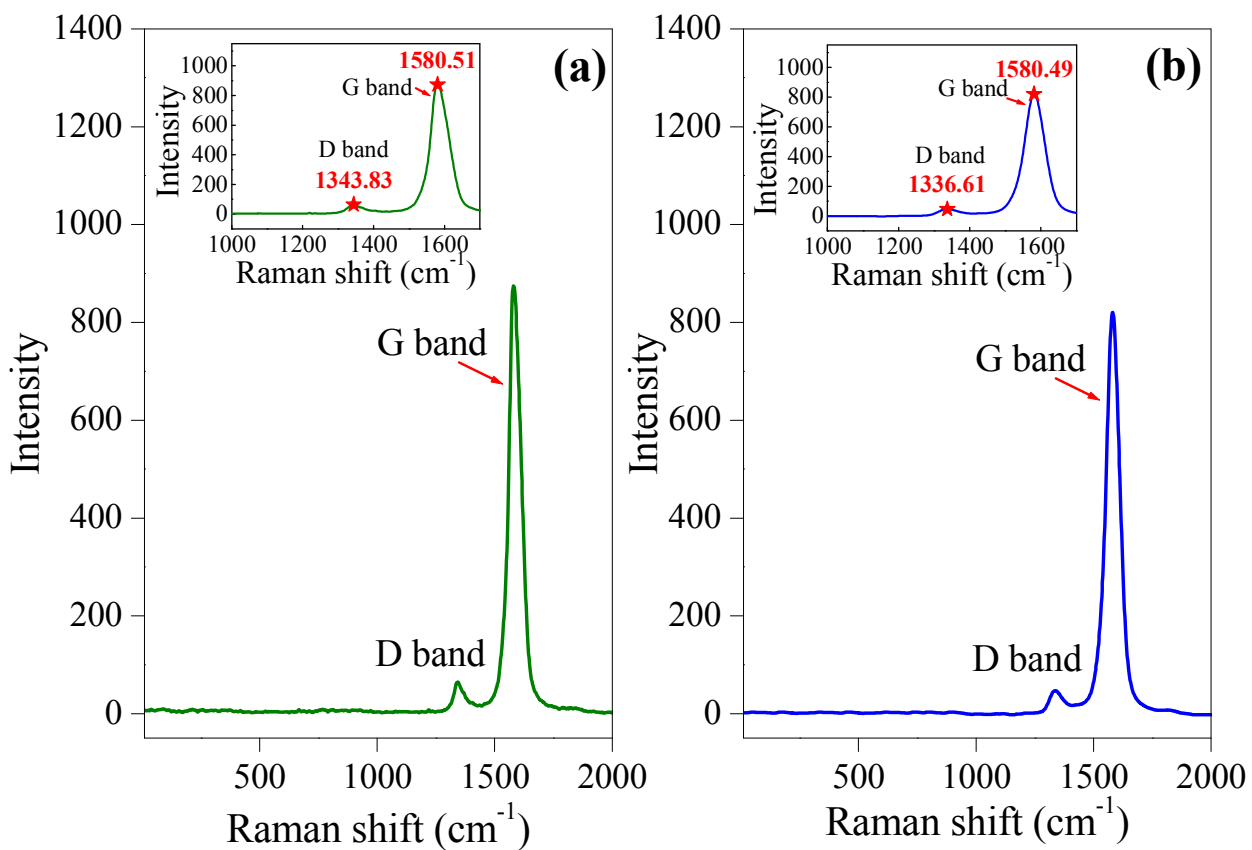


Fig. 4 Raman spectra of (a) MWCNTs (grown over Ni-Cr-KIT-6) and (b) MWCNTs (grown over Co-Cr-KIT-6).

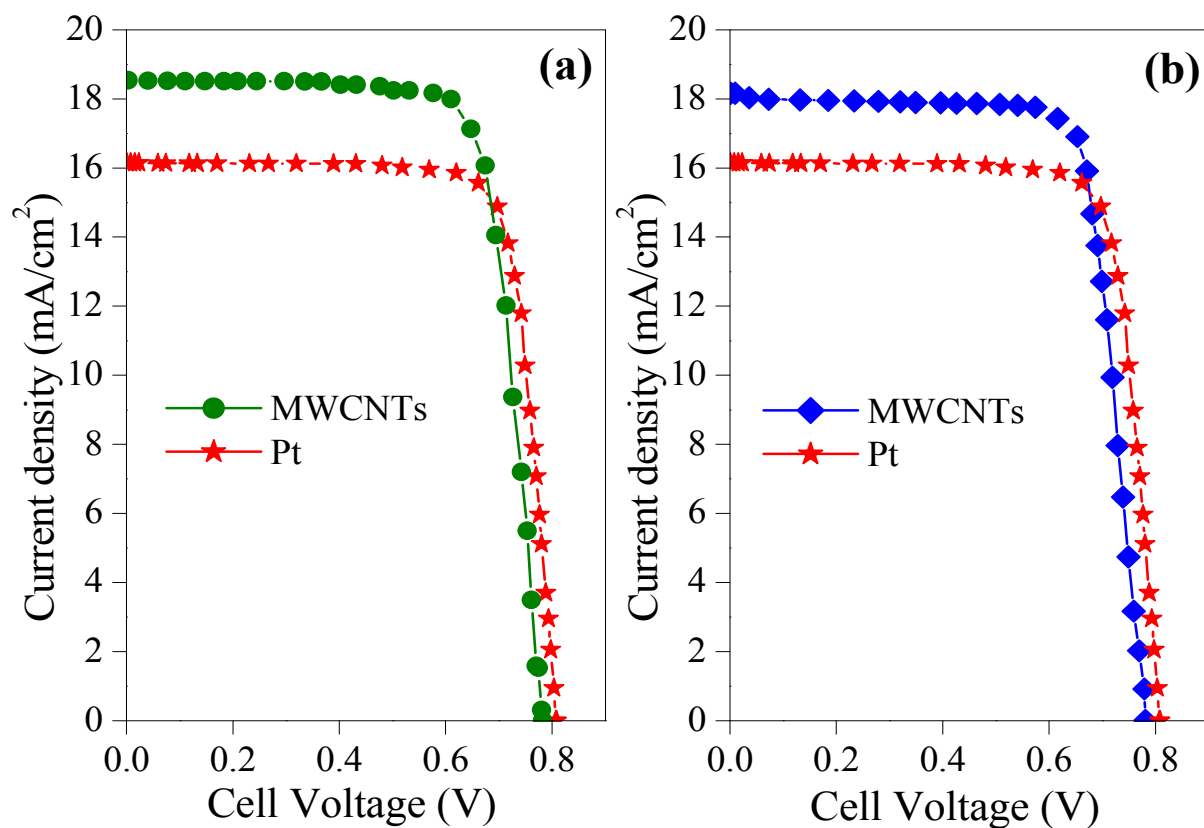


Fig. 5 Photocurrent density-cell voltage (J - V) performance of (a) Pt Vs MWCNT (grown over Ni-Cr-KIT-6) and (b) Pt Vs MWCNT (grown over Co-Cr-KIT-6) counter electrode DSSCs at $100 \text{ mW}/\text{cm}^2$ of simulated solar illumination.

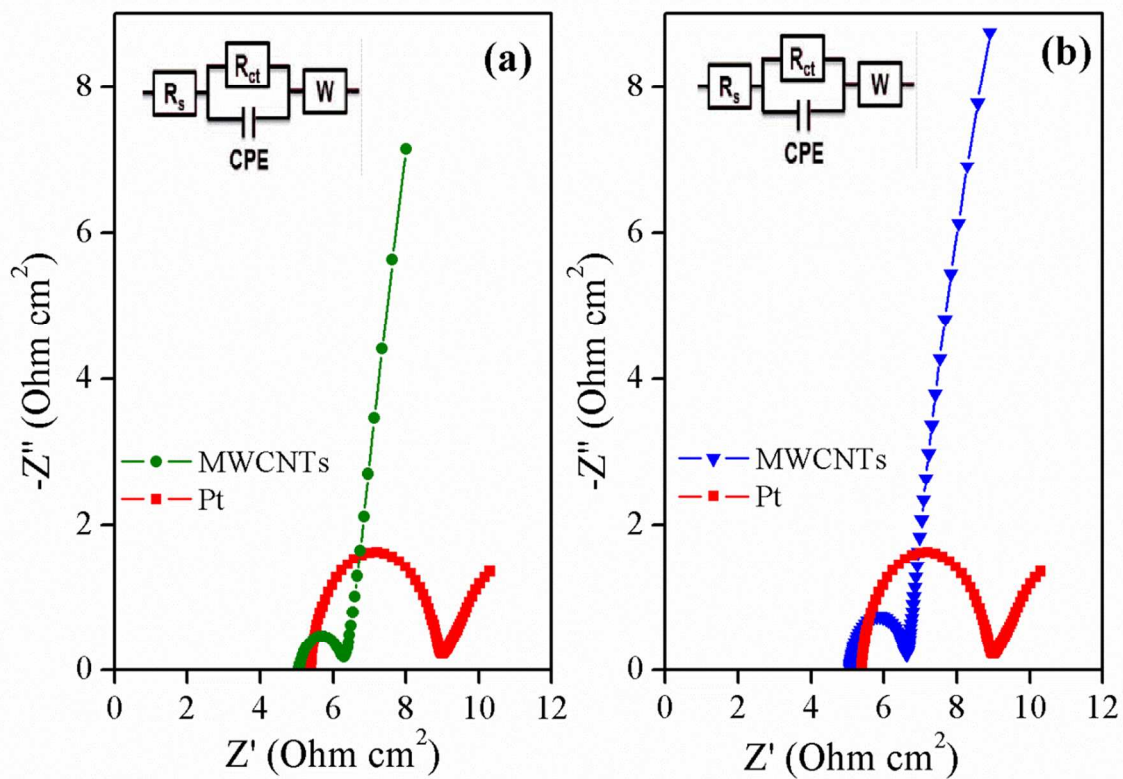


Fig. 6 Electrochemical impedance spectra of (a) Pt Vs MWCNTs (grown over Ni-Cr-KIT-6) and (b) Pt Vs MWCNTs (grown over Co-Cr-KIT-6).

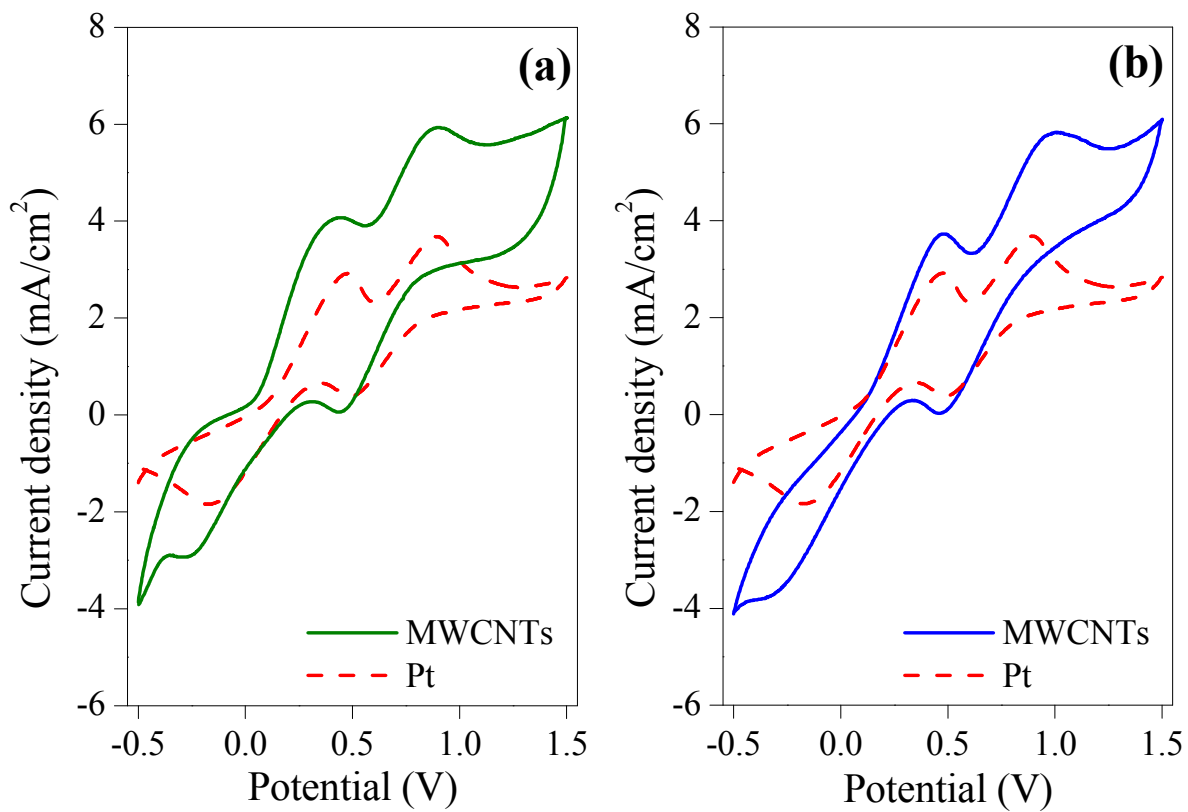


Fig. 7 Cyclic voltammograms of (a) Pt Vs MWCNT (grown over Ni-Cr-KIT-6) and (b) Pt Vs MWCNT (grown over Co-Cr-KIT-6) electrodes in acetonitrile solution containing 10 mM LiI + 1 mM I₂ + 0.1 M LiClO₄ at a scan rate of 25 mV/s.

Table 1 Electrochemical and photovoltaic parameters of DSSCs with Pt or MWCNT (grown over Ni-Cr-KIT-6 and Co-Cr-KIT-6) counter electrodes.

Counter electrode	R_{ct} ($\Omega \text{ cm}^2$)	J_{sc} (mA/cm^2)	V_{oc} (V)	FF (%)	η (%)
Pt	2.78	16.15	0.80	75.8	9.87
MWCNTs (grown over Ni-Cr-KIT-6)	0.74	18.54	0.79	75.7	10.53
MWCNTs (grown over Co-Cr-KIT-6)	0.81	18.16	0.78	75.9	10.44

Table 2 Photovoltaic parameters of DSSCs with different counter electrodes under 100 mW/cm² illumination.

Counter electrode	J_{sc} (mA/cm ²)	V_{oc} (V)	FF (%)	η (%)	Ref.
MWCNTs	18.23	0.74	67	9.05	33
MWCNT@RGONRs	16.87	0.70	59	6.91	34
CNFs	12.60	0.76	57	5.5	35
TiN-CNTs	12.74	0.75	57	5.41	36
NiS/MWCNT	14.18	0.75	74	7.90	37
VACNT/NC	13.36	0.80	68	7.26	38
Pt-MWCNTs	17.71	0.75	65	8.62	39
N-CNT	14.02	0.77	67	7.04	40
MWCNT@MoS ₂	13.69	0.73	65	6.45	41
EC/MWCNTs	12.12	0.76	75	6.97	42
P-BP	07.83	0.73	70	4.02	43
R-GONR/CNT	16.73	0.73	67	8.23	44
VACNTs/GP	14.24	0.68	62	6.05	45
VASWCNTs	12.66	0.61	68	5.25	46
Ni-CNT-CNF	15.83	0.80	63	7.96	47
Pt	16.15	0.80	75.8	9.87	This work
MWCNTs (grown over Ni-Cr-KIT-6)	18.54	0.79	75.7	10.53	This work
MWCNTs (grown over Co-Cr-KIT-6)	18.16	0.78	75.9	10.44	This work

CNFs – carbon nanofibres; RGONRs – reduced graphene oxide nanoribbon; TiN – titanium nitride; NC – nanocarbon; NiS – nickel sulfide; MoS₂ – molybdenum sulfide; EC – ethyl cellulose; VACNT – vertically-aligned CNT; P-BP – plasma-treated bucky paper; GP – graphene paper; VASWCNTs – vertically-aligned SWCNTs